Journal of Energy Storage 48 (2022) 103950

Contents lists available at ScienceDirect

Journal of Energy Storage

journal homepage: www.elsevier.com/locate/est

Optimum configuration of a metal foam layer for a fast thermal charging energy storage unit: A numerical study

S.A.M. Mehryan [a], Kasra Ayoubi Ayoubloo [b], Mahboobe Mahdavi [c], Obai Younis [d,e], Zahra Kazemi [f], Maryam Ghodrat [g], Mohammad Ghalambaz [h,i,*]

[a] Young Researchers and Elite Club, Yasooj Branch, Islamic Azad University, Yasooj, Iran
[b] Department of Mechanical Engineering, Shahid Chamran University of Ahvaz, Ahvaz, Iran
[c] Mechanical Engineering Department, Gannon University, 109 University Square, Erie, PA 16541, USA
[d] Department of Mechanical Engineering, College of Engineering at Wadi Addwaser, Prince Sattam Bin Abdulaziz University, Saudi Arabia
[e] Department of Mechanical Engineering, Faculty of Engineering, University of Khartoum, Sudan
[f] Department of Mechanical Engineering, Shiraz University, Shiraz 71936, Iran
[g] School of Engineering and Information Technology, University of New South Wales Canberra, Canberra 2610 ACT, Australia
[h] Metamaterials for Mechanical, Biomechanical and Multiphysical Applications Research Group, Ton Duc Thang University, Ho Chi Minh City, Vietnam
[i] Faculty of Applied Sciences, Ton Duc Thang University, Ho Chi Minh City, Vietnam

ARTICLE INFO

Keywords:
Melting heat transfer
Thermal energy storage
Metal foam
Optimization

ABSTRACT

The melting heat transfer of capric acid Phase Change Material (PCM) was numerically addressed in a channel shape Thermal Energy Storage (TES) unit. A combination of Cu nanoparticles and copper foam was used to improve the charging time of TES. A fixed amount of copper foam was applied to improve the heat transfer rate. The enthalpy-porosity approach, along with the finite element method, was used to simulate the free-convection melting heat transfer of composite PCM in the TES unit. Automatic time-step control and mesh adaptation technique were used to ensure the accuracy and convergence of the numerical solution. The porosity and the shape of the copper foam layer and volume fraction of nanoparticles were systematically optimized for minimum charging time using the Taguchi optimization approach. The results showed that a left right-hand triangle porous zone could lead to minimal charging time. The higher the porosity and volume fraction of nanoparticles, the lower the charging time. The combination of copper-foam, Cu nanoparticles, and optimum design of the porous layer reduced the melting time by three times. The optimal total charging time is reduced by 12.8% and 21.96% while changing the porous zone configuration from the RHT to REC and LHT.

1. Introduction

The phase change heat transfer has gained considerable attention during the past years due to its important applications in Thermal Energy Storage (TES) systems and Thermal Management Systems (TMS). The Phase Change Material (PCMs) are capable of storing/releasing a huge amount of thermal energy in the form of latent heat energy at a constant fusion temperature. The thermal energy storage properties of PCMs provide critical features for solar energy storage [1], transient systems thermal management [2], and the thermal load shifting in domestic [3, 4] and industrial [5] cooling and heating systems.

The practical drawback of PCMs is their poor thermal conductivity [6], which leads to a low heat transfer rate, affecting the charging and discharging time of a Thermal Energy Storage (TES) unit. Thus, various approaches such as extended surfaces and fins [7], nanoadditives [7, 8], metal foams [9–11], multi-layer PCMs [12], and heat pipes [13] have been employed to improve the heat transfer rate of PCMs.

Sheikholeslami [14] investigated the thermal energy release of a TES unit in the presence of extended surfaces and nanoadditives. The results showed that the presence of nanoadditives, CuO nanoparticles, improves the discharging time of the TES unit. The geometrical shape of the PCM container was also another important design parameter that could influence the discharging time. In another investigation, Sheikholeslami [15] revealed that the surface shape of heat transfer fluids' tubes is another important design variable that can improve the discharging of PCMs.

Mohammed et al. [16] employed metal foams to improve the charging response time of a TES unit. The PCM was embedded in an

* Corresponding author.
E-mail address: mohammad.ghalambaz@tdtu.edu.vn (M. Ghalambaz).

https://doi.org/10.1016/j.est.2021.103950
Received 16 August 2021; Received in revised form 19 December 2021; Accepted 31 December 2021
Available online 11 January 2022

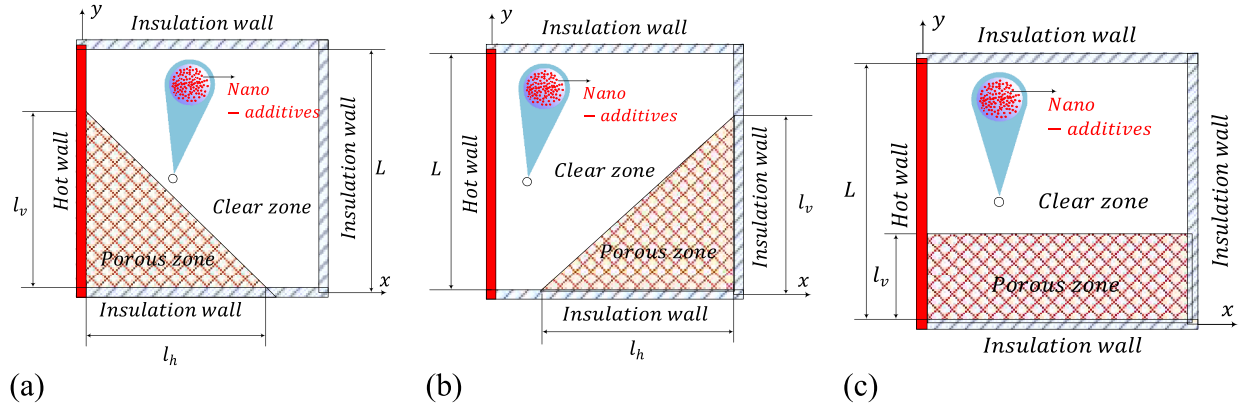

Fig. 1. Schematic view of the physical model and the metal foam configuration for three cases of (a): right-hand triangular porous medium (RHT); (b): left-hand triangular porous medium (LHT); (c): rectangular porous medium (REC).

Table 1
Specifications of the used material [55, 56].

Materials	Fusion temperature (°C)	Kinematic viscosity ($m^2\ s^{-1}$)	Latent heat (kJ kg^{-1})	Thermal expansion coefficient (K^{-1})	Thermal conductivity ($Wm^{-1}\ K^{-1}$)	Specific heat (kJ $kg^{-1}\ K^{-1}$)	Density (kg m^{-3})
Foam	//	//	//	//	380	0.386	8900
nano-additives	//	//	//	1.67e-5	401	0.385	8933
PCM	32	3e-6	152.7	1e-3	L*: 0.153 S: 0.372	L: 2.4 S: 1.9	L: 888 S: 1018

* L: Liquid, S: Solid

Table 2
Grid independency test details for a case with right-hand triangle porous insert and Cu nano additives. ($\varepsilon = 0.9$ and $\omega_{na} = 0.04$).

Cases	Number of domain/boundary elements	Time to run
Case I	2346/414	24min 32s
Case II	5098/435	1hr 2min 38s
Case III	**8005/459**	**1hr 50min 19s**
Case IV	16704/495	4hr 23min 14s
Case V	32848/607	9hr 32min 47s

electrical resistive metal foam, and thus, the heat generation could uniformly distribute in the PCM container and reduce the melting time by 21%. Talebizadeh et al. [17] analyzed the energy discharge of a copper foam heat exchanger filled by a PCM. Several air channels were placed in the PCM-copper foam enclosure. The air stream in the channels absorbs the latent heat and gets heated. The authors showed that improving the container's geometrical design could reduce the discharging time from 13.6 h to 6 h.

Yang et al. [18] experimentally and numerically studied the effect of aspect ratios of a tilted rectangular enclosure on the melting flow of a composite of a PCM and metal foam. They found that a cavity with a lower aspect ratio outperforms the one with a higher aspect ratio. In addition, the aspect ratio has not a significant influence on the melting process. In the other work, Yang et al. [19] used the combination of PCMs and metal foams to improve the charging response of a TES unit. The energy storage was a shell-tube heat exchanger where the heat transfer fluid was flowing, and the shell was filled with PCM-metal foam. The metal foam was made of open cells, so free convection heat transfer was possible. The presence of metal foam reduced the charging time by 64% compared to pure PCM.

Capric acid is an organic phase change PCM which can be embedded in metal foams [20]. This PCM has promising applications in building [21], solar [22], battery cooling [23], and other energy storage applications [24]. Low fusion temperature and the medium thermal conductivity of capric acid compared to other PCMs are the reasons that

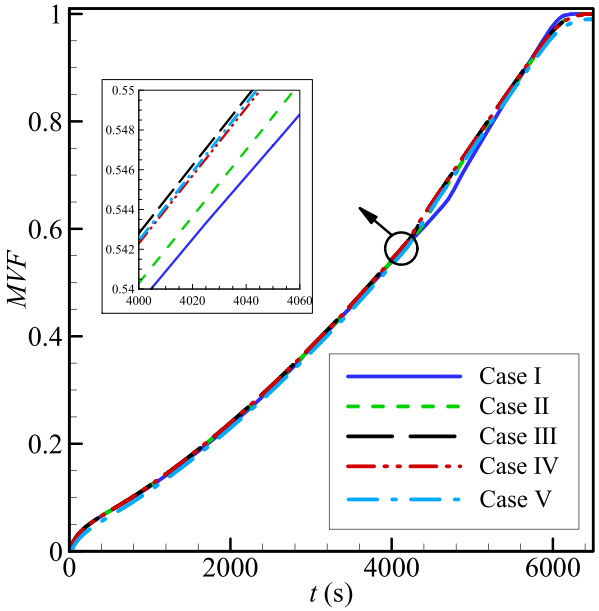

Fig. 2. The effect of mesh size on the *MVF* versus charging process time for *Cu*-additives when $\varepsilon = 0.9$, $\omega_{na} = 0.04$and the shape of the porous medium is a right-hand triangle in which $l_v = 40mm$

capric acid has been chosen for study. Moreover, Capric acid has good compatibility with nanoadditives [25, 26].

Esapour et al. [27] studied the melting and solidification heat transfer of paraffin (RT35) in a shell heat exchanger composed of multiple heat transfer tubes. The shell was fully filled with PCM and copper foam, while the heat transfer tubes were embedded inside the PCM-metal foam domain. The cool/hot water was flowing in the tubes to discharge/charge the TES unit. The authors found that the melting rate

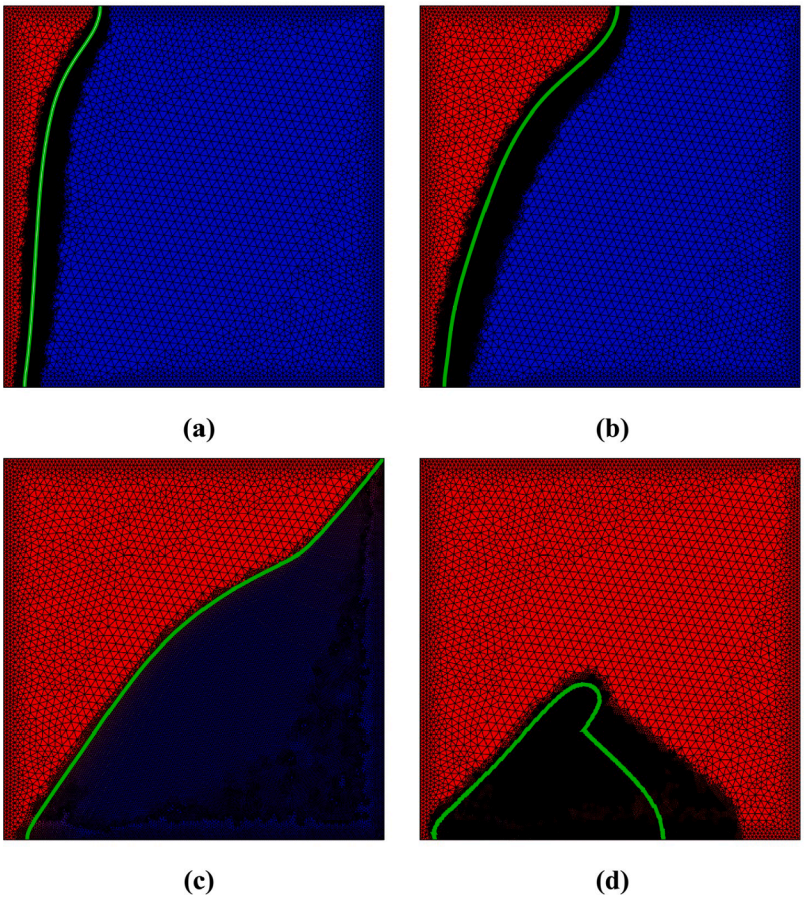

Fig. 3. Selected mesh Case III for the computations of the present study at various time steps with adaptations (a) $t = 1000$ s, (b) $t = 2000$ s, (b) $t = 4000$ s, and (d) $t = 6000$ s; the red color indicates the liquid region, blue shows the solid region, and the green line represents the melting interface for *Cu* nano-additives when $\varepsilon = 0.9$, $\omega_{na} = 0.04$ and the shape of the porous medium is a right-hand triangle in which $l_v = 40mm$

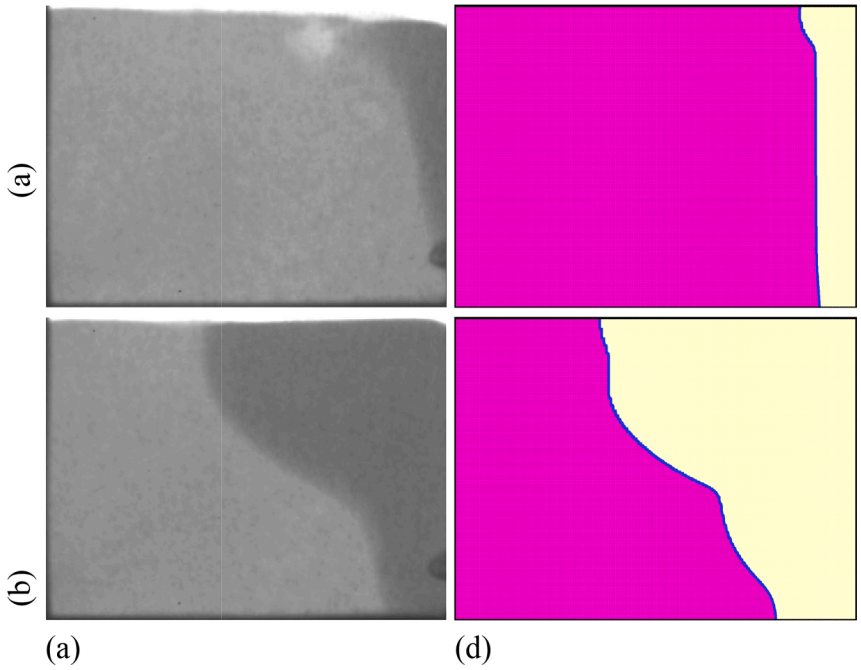

Fig. 4. The experimental melting images of Kumar et al. [46] (left column) and the current simulations (right column) for t= (a): 139s, and (b): 554s.

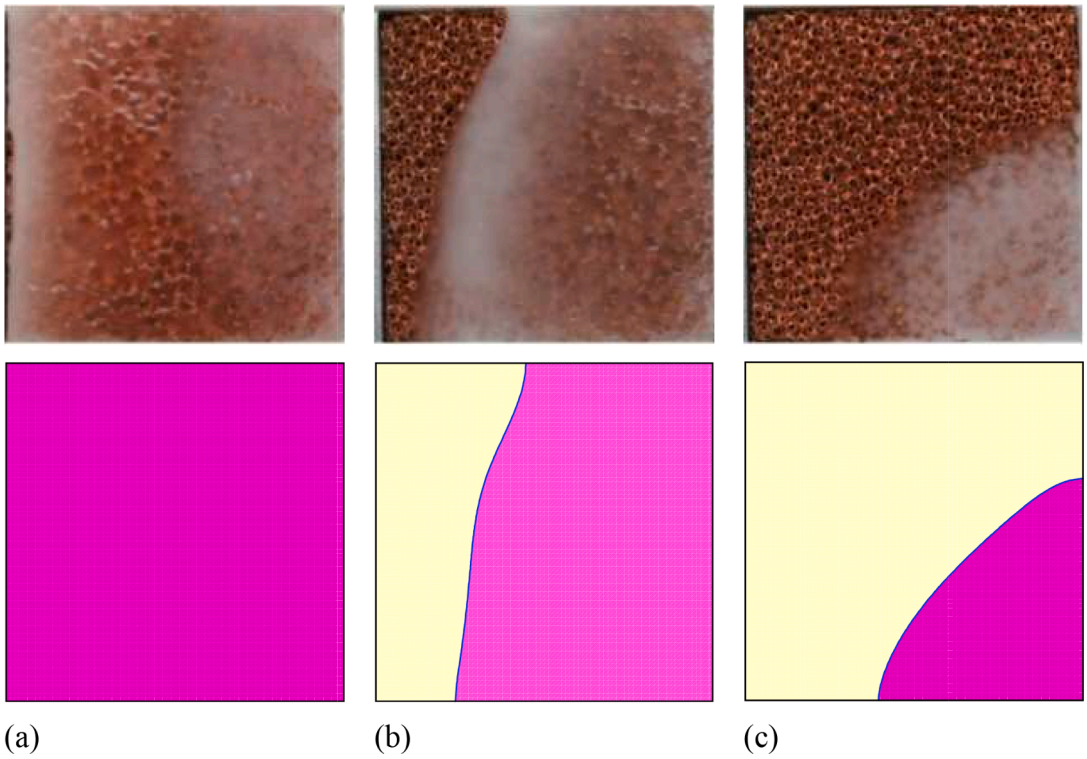

Fig. 5. The experimental images of [39] (top) and the present simulations (bottom) at various time steps of t= (a): 5400s (b): 10800s, and (c): 16200 s.

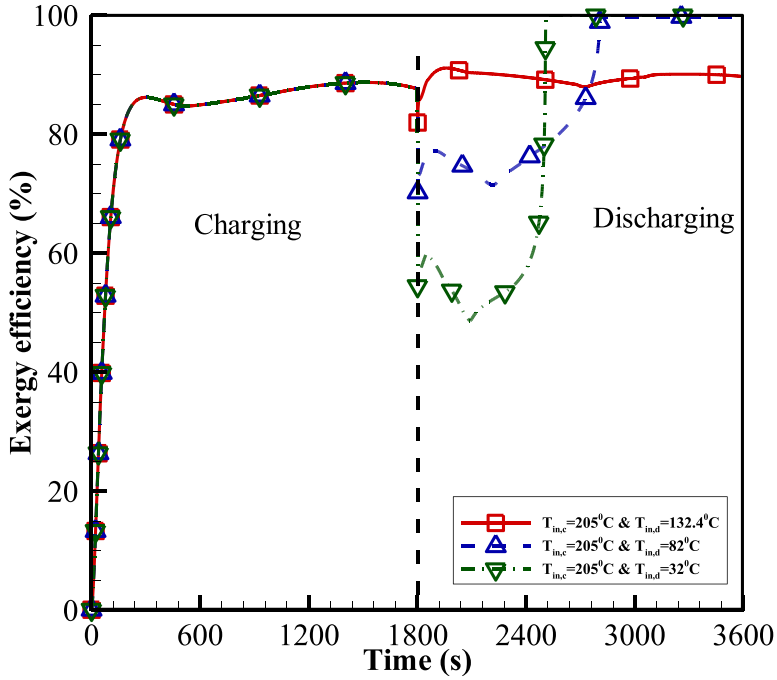

Fig. 6. The melting line of phase change, reported in the literature [47], and the current simulations. It is worth noting that $Fo = \alpha t/L^2$ and $Ste = C_{p,PCM}(T_h - T_{in})/h_{sf,PCM}$.

was not under the influence of the arrangement of tubes. The copper foam with a porosity of 0.9 reduced the charging time by 14%. Besides, the PCM-metal foam design was more sensitive to the number of utilized heat transfer tubes than pure PCM. Guo et al. [28] addressed the influence of a new fin-metal foam structure on the performance of a TES system. They observed that the fin-foam hybrid structure declines and increases the melting time and transient temperature response by 83.35% and 529.1% compared to a simple tube.

Employing metal foam improves the thermal conductivity of composite PCM-foam, notably. However, the metal foam suppressed the natural convection flow. Hence, the porous structure of metal foam acts as a barrier to advective heat transfer. Moreover, the metal foam does not contribute to latent thermal energy storage and could reduce the unit's total capacity with a fixed volume. As a result, some researchers

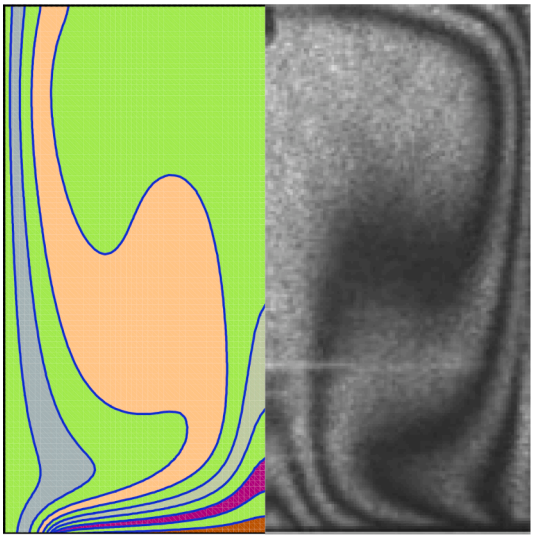

Fig. 7. The free convection isotherms of present simulation (first column) and experimental isotherms of [48] (second column).

attempted to improve TES units' heat transfer response by filling a portion of the enclosure with metal foam. In this regard, Zhu et al. [29] applied a partial layer of copper foam in a heatsink thermal management enclosure. The copper foam was filled with paraffin (RT40). The authors investigated the effect of the height of the foam layer in the heatsink. The results revealed that the porous layer's height reduces the heatsink temperature during transient high heat loads. Thus, the more metal foam, the better latent cooling thermal performance. However, the full filling of the heatsink by the copper foam did not significantly improve the cooling rate compared to partial filling. Thus, a partial-filling of the heatsink by the copper foam was found more advantageous compared to the full-filling of the heatsink.

Xu et al. [30] attempted to improve the thermal response of a tube shape TES using a fixed amount of metal foam. Their results showed that the metal insert should be continuously placed at the bottom of the enclosure. Thus, using the layer of metal foam, the energy storage time could be improved by 80%, and the melting rate was enhanced by 5.1 times.

The literature review shows that the geometrical design of a PCM enclosure and the shape of a porous layer could notably affect the thermal performance of a TES unit. Thus, the present study aims to address the impact of a partial layer of metal foam and nanoadditives on the thermal behavior and melting rate of a channel shape TES unit for the first time. The area of the metal foam layer was considered constant and the placement and geometry of the foam layer was changed. Then, the Taguchi optimization approach was employed to systematically find the optimized geometrical shape of the metal foam layer and volume fraction of nanoadditives.

2. Mathematical model

2.1. Model description

The configuration of the studied thermal energy storage unit is depicted in Fig. 1. Triangular or rectangular porous zones are placed inside a square container. The clear domain and pores of the porous medium are filled by capric acid, which is the selected as the phase change material (PCM). The shape of the porous medium can be right-hand triangular porous medium (RHT), left-hand triangular porous

Table 3
Taguchi L9 orthogonal table corresponding to range and levels of control parameters for the case of RHT.

Experiment number	Control Parameters			when $MVF = 1$ Melting time (s)	$ES(kJ/m)$	$P(kW/m)$	S/N Ratio
	ω_{na}	E	$l_v(mm)$				
1	0.00	0.8	32	3825	258.366	0.0675	-71.6526
2	0.00	0.9	36	7000	263.485	0.0376	-76.9020
3	0.00	1	40	10400	282.328	0.0271	-80.3407
4	0.04	0.8	36	6300	245.335	0.0389	-75.9868
5	0.04	0.9	40	6450	258.215	0.0401	-76.1912
6	0.04	1	32	9475	274.573	0.0290	-79.5316
7	0.08	0.8	40	5825	240.451	0.0413	-75.3059
8	0.08	0.9	32	4125	244.282	0.0592	-72.3085
9	0.08	1	36	8675	266.941	0.0308	-78.7654

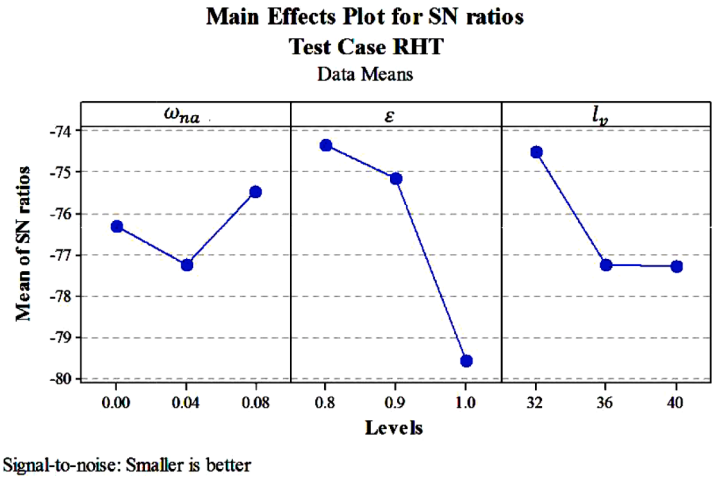

Fig. 8. Mean values of the S/N ratios for all the levels of the controlling parameters; test case RHT

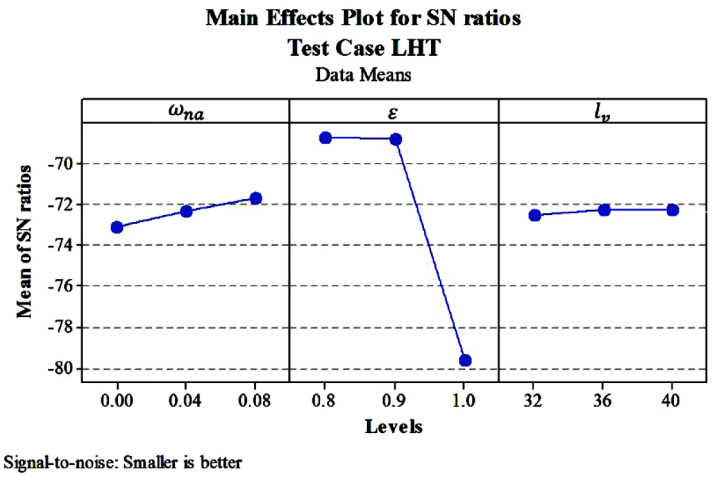

Fig. 9. Mean values of the S/N ratios for all the levels of the controlling parameters; test case LHT

Table 4
Taguchi L9 orthogonal table corresponding to range and levels of control parameters for the case of LHT.

Experiment number	Control Parameters			when $MVF = 1$ Melting time (s)	$ES(kJ/m)$	$P(kW/m)$	S/N Ratio
	ω_{na}	ε	$l_v(mm)$				
1	0.00	0.8	32	3025	269.953	0.0892	-69.6145
2	0.00	0.9	36	2925	276.367	0.0945	-69.3225
3	0.00	1	40	10475	282.239	0.0269	-80.4031
4	0.04	0.8	36	2725	262.920	0.0965	-68.7073
5	0.04	0.9	40	2700	269.462	0.0998	-68.6273
6	0.04	1	32	9525	274.408	0.0288	-79.5773
7	0.08	0.8	40	2450	255.221	0.1042	-67.7833
8	0.08	0.9	32	2625	261.370	0.0996	-68.3826
9	0.08	1	36	8700	266.639	0.0306	-78.7904

Table 5
Taguchi L9 orthogonal table corresponding to range and levels of control parameters for the case of REC.

Experiment number	Control Parameters			when $MVF = 1$ Melting time (s)	$ES(kJ/m)$	$P(kW/m)$	S/N Ratio
	ω_{na}	ε	$l_v(mm)$				
1	0.00	0.8	8	3350	268.798	0.08024	-70.5009
2	0.00	0.9	20	4000	275.629	0.06891	-72.0412
3	0.00	1	32	10400	282.393	0.02715	-80.3407
4	0.04	0.8	20	3400	261.506	0.07691	-70.6296
5	0.04	0.9	32	6000	264.051	0.04401	-75.5630
6	0.04	1	8	9500	274.515	0.02890	-79.5545
7	0.08	0.8	32	4825	246.772	0.05114	-73.6699
8	0.08	0.9	8	2925	260.697	0.08913	-69.3225
9	0.08	1	20	8650	266.609	0.03082	-78.7403

Table 6
The optimum values of the controlling parameters; test case RHT.

Optimum value	**Factor**			**Time When $MVF = 1$**	**Taguchi Value MVF Time**	***ES* (*kJ/m*)**	***P* (*kW/m*)**
	ω_{na}	ε	$l_v(mm)$				
	0.08	0.8	32	3300	3538.89	183.631	0.0556

Table 7
The rank values of the controlling parameters; test case RHT.

	ω_{na}	E	$l_v(mm)$
Level 1	-76.30	-74.32	-74.50
Level 2	-77.24	-75.13	-77.22
Level 3	-75.46	-79.55	-77.28
δ	1.78	5.23	2.78
Rank	3	1	2

medium (LHT), and rectangular porous medium (REC).

Cu nanoparticles are dispersed within the PCM with the purpose of improving its thermal characteristics. The left outer surface of the container is kept at a constant temperature of T_h ($T_h = 42$), which is more than the fusion temperature of the phase change substance ($T_{fu} = 32$). The rest of the container walls are all insulated. The thermophysical specifications of the materials involved in the problem are listed in Table 1. The surface area of the porous medium is the same for all the cases. Thus, the surface area of the porous medium is a constraint in this study. As a result, when l_v changes, l_h should vary to keep the surface

Table 8
The optimum values of the controlling parameters; test case LHT.

Optimum value	Factor			Time When $MVF = 1$	Taguchi Value MVF Time	ES (kJ/m)	P (kW/m)
	ω_{na}	ε	$l_v(mm)$				
	0.08	0.9	40	2575	2516.67	262.271	0.1018

Table 9
The rank values of the controlling parameters; test case LHT.

	ω_{na}	E	l_v(mm)
Level 1	-73.1134	-68.7017	-72.5248
Level 2	-72.304	-68.7775	-72.2734
Level 3	-71.6521	-79.5903	-72.2712
δ	1.461271	10.88854	0.253572
Rank	2	1	3

area constant. Metal foams are typically produced in rectangular shape cubes. Cutting and producing metal foams with straight cutting-path is a production advantage. Producing a triangular shape or a rectangular shape is possible by performing just one straight cutting action. Hence, the triangular and rectangular shapes were adopted in the present study.

2.2. Governing equations and boundary conditions

The governing equations, including the continuity, momentum, and energy equations, are expressed below [31–33]. The enthalpy-porosity technique is implemented to simulate the melting within the PCM.

$$\nabla\cdot\vec{V}=0 \tag{1}$$

$$\frac{\rho_{NeP,l}}{\varepsilon_r^2}\left[\varepsilon_r^{-1}\frac{\partial u}{\partial t}+\left(\vec{V}\cdot\nabla\right)u\right]+\frac{\partial p}{\partial x}-\frac{\mu_{NeP,l}}{\varepsilon_r}\nabla^2u+\frac{\mu_{NeP,l}}{K_r}u+A_{mush}\frac{(1-\delta(T))^2}{\delta^3(T)+\varsigma}u=0 \tag{2}$$

$$\frac{\rho_{NeP,l}}{\varepsilon_r^2}\left[\varepsilon_r^{-1}\frac{\partial u}{\partial t}+\left(\vec{V}\cdot\nabla\right)v\right]+\frac{\partial p}{\partial y}-\frac{\mu_{NeP,l}}{\varepsilon_r}\nabla^2v+\frac{\mu_{NeP,l}}{K_r}v+A_{mush}\frac{(1-\delta(T))^2}{\delta^3(T)+\varsigma}v-\rho_{NeP,l}g\beta_{NeP,l}\left(T-T_{fu}\right)=0 \tag{3}$$

in which,

$$\delta(T)=\begin{cases}0 & T<T_{fu}-\Delta T/2\\ \dfrac{T-T_{fu}}{\Delta T}+\dfrac{1}{2}T_{fu}-\Delta T/2<T<T_{fu}+\Delta T/2\\ 1 & T>T_{fu}+\Delta T/2\end{cases} \tag{4}$$

Also, ε_r and K_r are defined as the following.

$$\varepsilon_r=\begin{cases}\varepsilon & r=\mathbf{1}\\ 1 & r=\mathbf{2}\end{cases},\quad K_r=\begin{cases}K & r=\mathbf{1}\\ \infty & r=\mathbf{2}\end{cases} \tag{5}$$

where in $r = 1$ and 2 denote the porous and clear zones, respectively. ε is the porosity of the porous regions, and K is the permeability of the porous zone and can be calculated using Eqs. (6a)-(6c).

$$K=d_p^2\frac{73\times10^{-5}}{(1-\varepsilon)^{0.224}}\left(d_ld_p^{-1}\right)^{-1.11} \tag{6a}$$

Table 11
The rank values of the controlling parameters; test case REC.

	ω_{na}	ε	$l_v(mm)$
Level 1	-74.29	-71.60	-73.13
Level 2	-75.25	-72.31	-73.80
Level 3	-73.91	-79.55	-76.52
δ	1.34	7.95	3.40
Rank	3	1	2

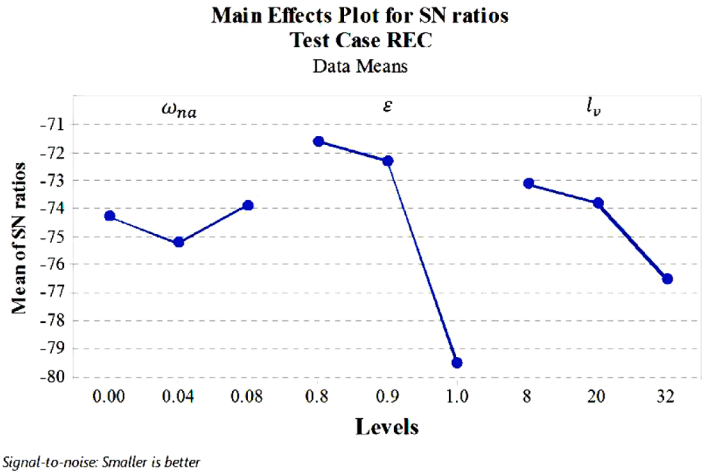

Fig. 10. Mean values of the S/N ratios for all the levels of the controlling parameters; test case REC

Table 10
The optimum values of the controlling parameters; test case REC.

Optimum value	Factor			Time when $MVF = 1$	Taguchi Value MVF Time	ES (kJ/m)	P (kW/m)
	ω_{na}	ε	$l_v(mm)$				
	0.08	0.8	8	2875	2794.44	254.236	0.0884

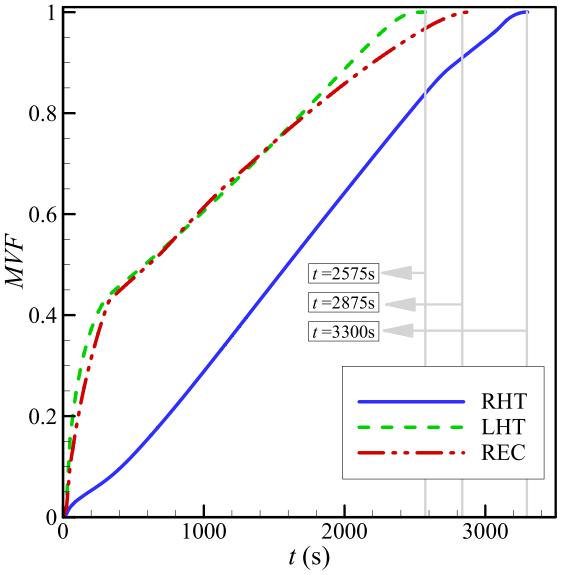

Fig. 11. Effect of the location of the porous insert on the melting volume fraction (*MVF*) in cases with *Cu* nano-additives at optimum values as shown in Tables 6, 8 and 10.

$$\frac{d_l}{d_p} = 1.18\left(\frac{1-\varepsilon}{3\pi}\right)^{0.5}\left[1-\exp(-(1-\varepsilon)/0.04)\right]^{-1} \tag{6b}$$

in which,

$$d_p = 254\times 10^{-4}\omega^{-1}(PPI) \tag{6c}$$

$$(\rho C_p)_r\frac{\partial T}{\partial t} + (\rho C_p)_{NeP,l}\left(\vec{V}\cdot\nabla\right)T = \nabla\cdot(\lambda_r\nabla T) - \rho_{NeP,l}h_{sf,NeP}\varepsilon_r\frac{\partial\delta(T)}{\partial t} \tag{7}$$

where,

$$(\rho C_p)_r = \begin{cases}(\rho C_p)_{pm,eff} & r=\mathbf{1}\\ (\rho C_p)_{NeP} & r=\mathbf{2}\end{cases} \tag{8}$$

in which,

$$(\rho C_p)_{pm,eff} = \chi(T)(\rho C_p)_{pm,eff,l} + (1-\chi(T))(\rho C_p)_{pm,eff,s} \tag{9a}$$

$$(\rho C_p)_{pm,eff,i} = (1-\varepsilon_k)(\rho C_p)_{sm} + \varepsilon_k(\rho C_p)_{NeP,i} \tag{9b}$$

i refers to the liquid and solid states of the NePCM. λ_r of the Eq. (7) is:

$$\lambda_r = \begin{cases}\lambda_{pm,eff} r=1\\ \lambda_{NeP} r=2\end{cases} \tag{10}$$

in which,

$$\lambda_{pm,eff} = \chi(T)\lambda_{pm,eff,l} + (1-\chi(T))\lambda_{pm,eff,s} \tag{11a}$$

$$\lambda_{NeP} = \chi(T)\lambda_{NeP,l} + (1-\chi(T))\lambda_{NeP,s} \tag{11b}$$

The literature review shows that many relations can be used to estimate the thermal conductivity of the porous zones [34]. For example, literature works used empirical correlations by Bhattacharya et al. [35] or analytical models by Yang et al. [36, 37]. In the current study, which is in good agreement with our test cases [38, 39]:

$$\lambda_{pm,eff,i} = \frac{\left[\lambda_{NeP,i}+\pi\left(\sqrt{\chi}-\chi\right)\Delta\lambda\right]\left[\lambda_{NeP,i}+(\chi\pi)\Delta\lambda\right]}{\lambda_{NeP,i}+\left[\frac{4}{3}\sqrt{\chi}(1-\varepsilon)+\pi\sqrt{\chi}-(1-\varepsilon)\right]\Delta\lambda} \tag{12a}$$

in which,

$$\chi = \frac{1-\varepsilon}{3\pi}, \Delta\lambda = \lambda_{sm} - \lambda_{NeP,i} \tag{12b}$$

The thermophysical specifications of the composite, i.e. NePCM, can be listed as the following:

Density:

$$\rho_{NeP} = \rho_{PCM} + \omega_{na}(\rho_{na} - \rho_{PCM}) \tag{13a}$$

$$\rho_{PCM}(T) = \rho_{PCM,l}\chi(T) + (1-\chi(T))\rho_{PCM,s} \tag{13b}$$

Dynamic viscosity:

$$\mu_{NePCM,l} = \mu_{PCM,l}(1-\omega_{na})^{-2.5} \tag{14}$$

Thermal-volume expansion coefficient:

$$\rho_{NeP,l}\beta_{NeP,l} = \rho_{PCM,l}\beta_{PCM,l} + \omega_{na}\left(\rho_{na}\beta_{na} - \rho_{PCM,l}\beta_{PCM,l}\right) \tag{15}$$

Thermal conductivity:

$$\frac{\lambda_{NeP,i}}{\lambda_{PCM,i}} = \frac{\left(\lambda_{na}+2\lambda_{PCM,i}\right) - 2\omega_{na}\left(\lambda_{PCM,i}-\lambda_{na}\right)}{\left(\lambda_{na}+2\lambda_{PCM,i}\right) + \omega_{na}\left(\lambda_{PCM,i}-\lambda_{na}\right)} \tag{16}$$

Heat capacity:

$$\rho_{NeP}C_{p,NeP} = \rho_{PCM}C_{p,PCM} + \omega_{na}\left(\rho_{na}C_{p,na} - \rho_{PCM}C_{p,PCM}\right) \tag{17a}$$

$$\rho_{PCM}C_{p,PCM}(T) = \rho_{PCM,l}C_{p,PCM,l}\chi(T) + (1-\chi(T))\rho_{PCM,s}C_{p,PCM,s} \tag{17b}$$

Latent heat:

$$\rho_{NeP,l}h_{sf,NeP} = (1-\omega_{na})\rho_{PCM,l}h_{sf,PCM} \tag{18}$$

The controlling boundary conditions for the above-presented physics are as follows:

On the borders of clear and porous domains:

$$T|_{cz} = T|_{pz}, \lambda_{NeP}\left.\frac{\partial T}{\partial n}\right|_{cz} = \lambda_{pm,eff}\left.\frac{\partial T}{\partial n}\right|_{pz} \tag{19a}$$

On the left horizontal border:

$$u = v = 0, T = T_h \tag{19b}$$

On the rest borders:

$$u = v = 0, \frac{\partial T}{\partial n} = 0 \tag{19c}$$

n of the above relation is x and y for the vertical and horizontal walls.

The energy stored in the composite can be divided into two parts; sensible and latent energies.

$$ES = \int_A (\rho C_p)_r(T-T_{in})dA + \int_A \rho_{NeP,l}h_{sf,NeP}\varepsilon_r dA \tag{20}$$

The first and second terms of the right side of the above relation denote the sensible and latent energies, respectively. T_{in} is the initial temperature of the domain and considered to be 22°C. Moreover, the melted volume fraction keeping the latent heat is:

$$MVF = \frac{\int_A \varepsilon_r\chi(T)dA}{\int_A \varepsilon_r dA} \tag{21}$$

3. Numerical approach, grid dependency test, and validation

3.1. Mesh adaptation and numerical method

In order to model the phase change problem in this study, two main source terms need to be introduced. First, the velocity source term of the momentum formula, $A_{mush}[(1-\delta(T))^2/\delta^3(T)+\varsigma](u,v)$ controlling the velocity vector of solid/liquid interface area. This term is defined based

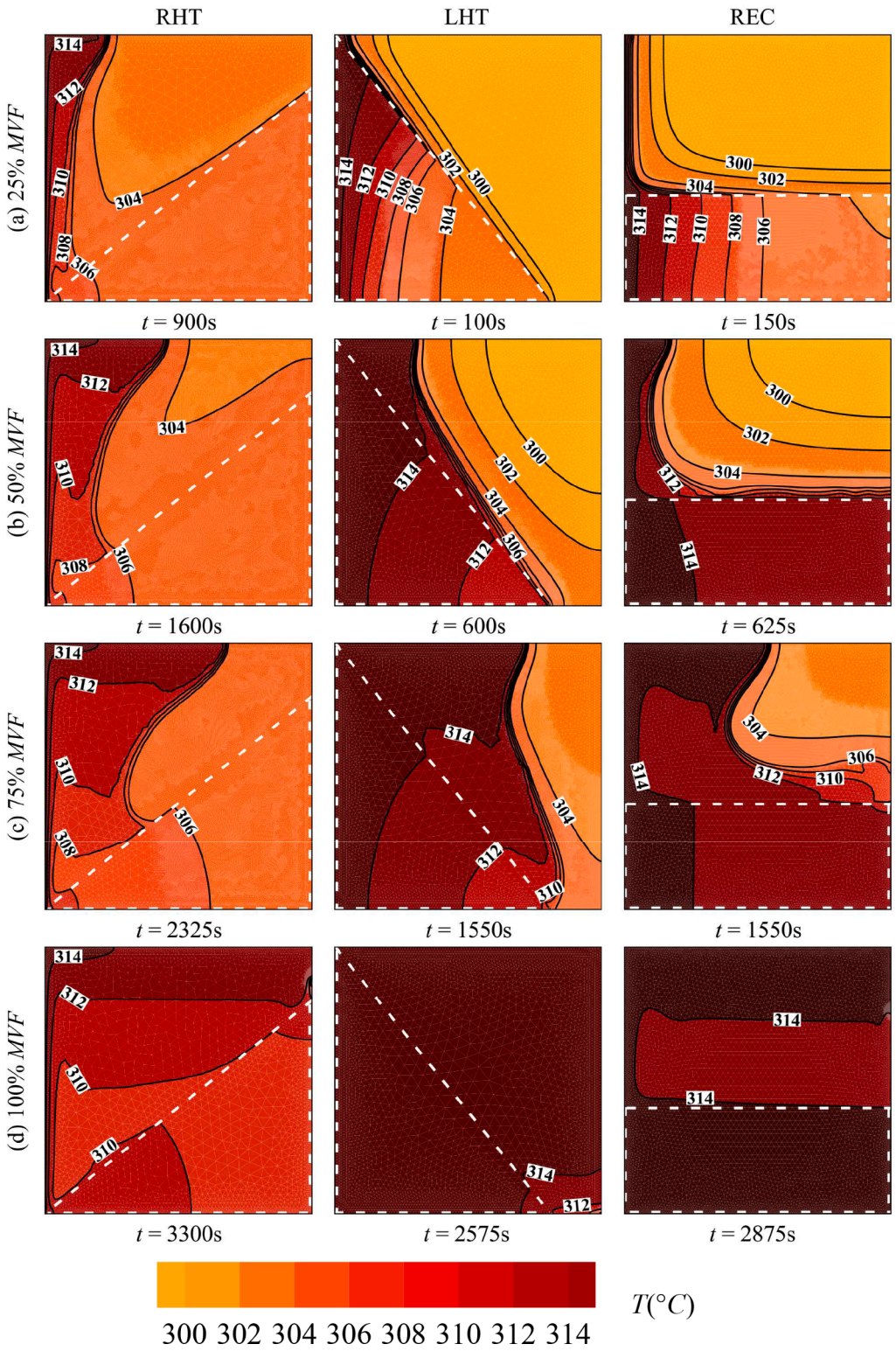

Fig. 12. Temperature contours of optimum values for different state of porous zones with specific percent of melting progress at different times for *Cu* nano-additives

on the domain temperature (T). While the fusion temperature is higher than the domain temperature, this term reaches a large value in this area leading to stopping the liquid flow. Second, the energy sink related to the latent heat of fusion, i.e., $\partial\delta/\partial T$, playing an important role. The phase domain is controlled by this term during the fusion temperature of the domain study (constant temperature). It is needed to take into account the considerable variations of momentum and heat equations during the solidification and melting interface zone. So, a high quality and resolution grid is essential in this area.

Also, the interface of solidification/melting area within the domain study is not big because of the effects of natural convection inside the enclosure and the low thermal conductivity of PCMs. By the help of the fusion temperature range, ΔT, its thickness is controlled. It is physically anticipated that a small amount of ΔT leads to a very thin solidification/melting interface zone. These specifications of the solidification/melting area make it clear that a highly intense grid is essential in this thin area

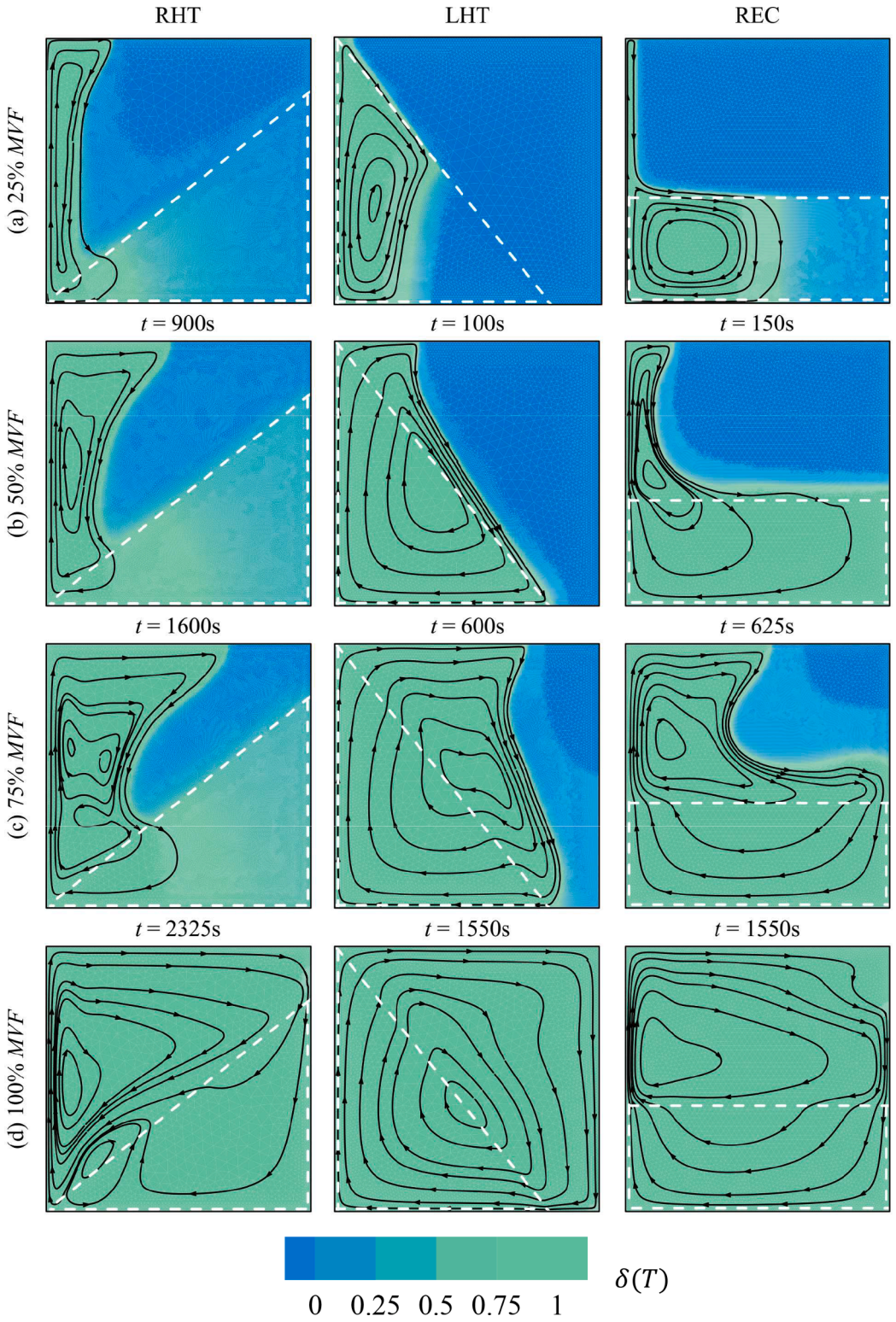

Fig. 13. Streamlines of optimum values for different states of porous zones with specific percent of melting progress at different times for *Cu* nano-additives

leading to a very costly and time-consuming numerical computations. So, in order to capture the phase change phenomena around this zone, mesh adaption is used, contributing to low-cost with high-resolution numerical computations.

Considering the fusion source term, i.e., $\partial\delta(T)/\partial T$, is found that δ is temperature dependent. Thus, the quality of the grid inside the domain study and the chosen time step are vital. As said, the computation time increases due to the use of a dense mesh. However, it occurs when a non-dense mesh is utilized because of smaller time-step leading to more computational time. All in all, both mesh adaption and correct time are achieved by choosing an automatic time-step.

The controlling equations as well as the boundary and initial conditions are solved by developing a Finite Element Method (FEM). Also, in order to control the mushy zone, the solid/region area, from mesh adoption and velocity viewpoint, user-defined codes are written. The velocity, pressure, and temperature equations are expanded by the basis

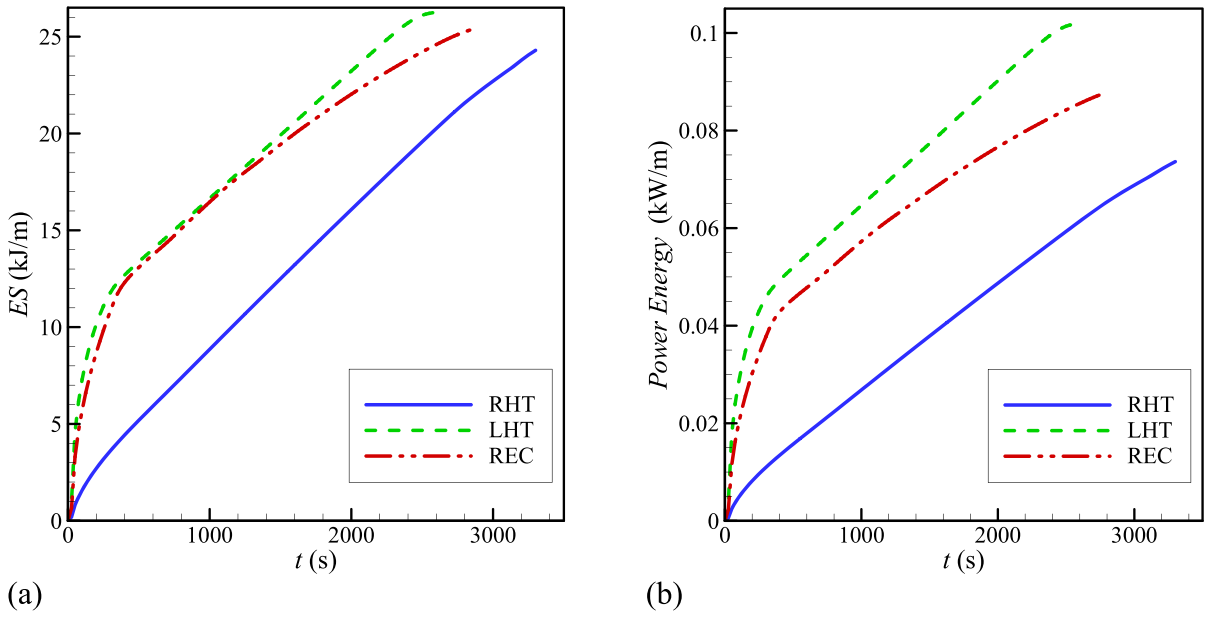

Fig. 14. Effect of (a) total energy stored (*ES*) and (b) power energy stored during time for *Cu* nano-additives at optimum values, shown in Tables 6, 8, and 10.

set $\{N_i\}_{i=1}^{M}$, and the governing equations are transformed to a weak form.

$$(u,v,p,T) \approx \sum_{m=1}^{M}[u,v,p,T]N_m(x,\ y) \tag{22}$$

Galerkin finite element method is invoked for this study. By this method, residual functions at nodes of the computational zone are used to rewrite the governing equations. Also, by linear shape functions, the temperature, velocity, and pressure are expanded. *N*, i.e. the basis function, is the same for all parameters.

$$R_k^1 \approx \sum_{m=1}^{M} u_m \int \frac{\partial N_m}{\partial x} N_k dydx + \sum_{m=1}^{M} v_m \int \frac{\partial N_m}{\partial y} N_k dydx \tag{23a}$$

$$R_k^2 \approx \frac{\rho_{NeP,l}}{\varepsilon_r}\sum_{m=1}^{M} u_m \int \frac{\partial N_m}{\partial t} N_k dydx + \frac{\rho_{NeP,l}}{\varepsilon_r^2}\sum_{m=1}^{M} u_m \int \begin{bmatrix} \left(\sum_{m=1}^{M} u_m N_m\right)\frac{\partial N_m}{\partial x} \\ +\left(\sum_{m=1}^{M} v_m N_m\right)\frac{\partial N_m}{\partial y} \end{bmatrix} N_k dydx$$
$$+\sum_{m=1}^{M}\int\left(-\sum_{m=1}^{M} p_m N_m\right)\frac{\partial N_m}{\partial x} N_k dydx + \frac{\mu_{NeP,l}}{\varepsilon_r}\sum_{m=1}^{M} u_m \int \frac{\partial N_m}{\partial x}\frac{\partial N_k}{\partial x} dydx$$
$$+\frac{\mu_{NeP,l}}{\varepsilon_r}\sum_{m=1}^{M} u_m \int \left[\frac{\partial N_m}{\partial y}\frac{\partial N_k}{\partial y}\right] dydx - \frac{\mu_{NeP,l}}{\varepsilon_r}\int\left(\sum_{m=1}^{M} u_m N_m\right) N_k dydx$$
$$-A_{mush}\frac{(1-\delta(T))^2}{\delta^3(T)+\varsigma}\int\left(\sum_{m=1}^{M} u_m N_m\right) N_k dydx \tag{23b}$$

$$R_k^3 \approx \frac{\rho_{NeP,l}}{\varepsilon_r}\sum_{m=1}^{N} v_m \int \frac{\partial N_m}{\partial t} N_k dydx + \frac{\rho_{NeP,l}}{\varepsilon_r^2}\sum_{m=1}^{N} v_m \int \begin{bmatrix} \left(\sum_{m=1}^{N} u_m N_m\right)\frac{\partial N_m}{\partial x} \\ +\left(\sum_{m=1}^{N} v_m N_m\right)\frac{\partial N_m}{\partial y} \end{bmatrix} N_k dydx$$
$$+\sum_{m=1}^{N}\int\left(-\sum_{m=1}^{N} p_m N_m\right)\frac{\partial N_m}{\partial y} N_k dydx + \frac{\mu_{NeP,l}}{\varepsilon_r}\sum_{m=1}^{N} v_m \int \frac{\partial N_m}{\partial x}\frac{\partial N_k}{\partial x} dydx$$
$$+\frac{\mu_{NeP,l}}{\varepsilon_r}\sum_{m=1}^{N} v_m \int \left[\frac{\partial N_m}{\partial y}\frac{\partial N_k}{\partial y}\right] dydx - \frac{\mu_{NeP,l}}{\varepsilon_r}\int\left(\sum_{m=1}^{N} v_m N_m\right) N_k dydx$$
$$-A_{mush}\frac{(1-\delta(T))^2}{\delta^3(T)+\varsigma}\int\left(\sum_{m=1}^{N} v_m N_m\right) N_k dydx + \rho_{NeP,l} g\beta_{NeP,l}\left(\int\left(\sum_{m=1}^{N} T_m N_m\right) N_k dxdy - T_{fu}\right) \tag{23c}$$

$$R_k^4 \approx (\rho C_p)_r \sum_{m=1}^{M} \mathrm{T}_m \int \frac{\partial N_m}{\partial t} N_k dydx$$
$$+ (\rho C_p)_{NeP,l} \sum_{m=1}^{M} \mathrm{T}_m \int \left[\left(\sum_{m=1}^{M} u_m N_m \right) \frac{\partial N_m}{\partial x} + \left(\sum_{m=1}^{M} v_m N_m \right) \frac{\partial N_m}{\partial y} \right] N_m dydx$$
$$+ \lambda_r \sum_{m=1}^{M} \mathrm{T}_m \int \left[\frac{\partial N_m}{\partial x}\frac{\partial N_k}{\partial x} + \frac{\partial N_m}{\partial y}\frac{\partial N_k}{\partial y} \right] dydx - \rho_{NeP,l} h_{sf,NeP} \varepsilon_r \sum_{m=1}^{M} \frac{\partial \delta(T_m)}{\partial T} \int \frac{\partial N_m}{\partial t} N_k dydx \quad (23d)$$

where

$$\frac{\partial \delta(T)}{\partial T} = \begin{cases} 0 & T \le T_{fu} - 0.5\Delta T \\ \dfrac{1}{\Delta T} & T_{fu} - 0.5\Delta T < T < T_{fu} + 0.5\Delta T \\ 0 & T \ge T_{fu} + 0.5\Delta T \end{cases} \quad (24)$$

Second-order Gaussian-quadrature method is used to integrate the residual equations. The complete information around Galerkin finite element method is expressed in [40, 41].

δ^* as a phase-field variable plays the role of the bound for grid adaptation, so $\delta^* = 1$ is the mesh adaptation space-domain. The temperature rate is considered at a wider domain of $3\Delta T/2$ against ΔT. This wider fusion domain makes the solidification/melting zone bigger, contributing to the smooth mesh transient in this area. $\delta^* = 1$ makes the refined mesh in the domain study five-times smaller compared to the regular mesh. δ^* is expressed as:

$$\delta^*(T) = \begin{cases} 0 & T \le T_{fu} - 1.5\Delta T \\ 1 & T_{fu} - 1.5\Delta T < T < T_{fu} + 1.5\Delta T \\ 0 & T \ge T_{fu} + 1.5\Delta T \end{cases} \quad (25)$$

Furthermore, the grid is sufficient while the interface of phase change locates within the adoption domain. So, the adoption procedure decreases by a wider adoption region around the interface. As the grid adoption of a larger domain leads to a higher number of grid elements and cost of computation, this high-cost computational step can be replaced with a larger grid-adaptation domain. This makes the used approach computationally effective.

3.2. Grid independence test and time step

Accurate and correct results of numerical investigations depend on the proper grid of domain study. In order to achieve the best mesh, grid-independency is carried out in the current study by examining five meshes containing different element numbers. Table 2 shows five cases of adopted grids with various domain and boundary elements provided for this study. The case study of grid independency test is the right hand triangular porous insert with the following parameters: $\varepsilon = 0.9$, $\omega_{na} = 0.04$ and $l_v = 40mm$

The melt volume fraction (MVF) at different time steps of the charging process is examined as the case of comparison of all grid cases. It can be seen a negligible difference among five cases, especially for cases III, IV, and V (Figs. 2 and 3). Considering the computational time, it is evident that the number of domain/boundary elements of case III is adequate for the numerical calculations.

In order to control the time-step in the current study, the free step Backward Differentiation Formula (BDF) as an automatic time step in the range order of one-two is used [42]. Newton method using a PARallel DIrect SOlver (PARDISO) solver [43–45] is utilized to solve the residual Eq. (25), with a residual error O(10^{-6}) and Newtonian damping factor of 0.8.

3.3. Validation

In order to validate the results of the present study, former related numerical and experimental investigations are considered to be compared. First, The interface of solid/liquid during melting of lead performed by Kumar et al. [46] experimentally is considered as the validation case. Their results were obtained by the flux neutron radiography. The vertical sidewalls were exposed a heat flux. However, the other walls were with no heat flux. The comparison of the melting front of the current investigation and those of Ref. [46] are demonstrated in Fig. 4 . The governing parameters in this comparison are $Ra = 14 \times 10^6$, $Ste = 4 \times 10^{-1}$, and $Pr = 236 \times 10^{-4}$. A good agreement is evident between the results of the two studies. Afterward, the experimental data of the research of Zheng et al. [39] is utilized to prove the correctness of the outcomes of the current work. They investigated around the heat transfer of melting phenomena within a square metal foam cavity embedded with paraffin wax. The pores of porous cavity having the size of o.1 m and porosity of o.95 were occupied with paraffin composite phase change material. The enclosure's left wall was exposed a heat flux of 1150 W/m^2. To compare the experimental results of Ref. [39] and present research, three-time steps are captured, and the interfaces of liquid/solid in the melting process are demonstrated in Fig. 5. As seen, the shape of the interface of both studies is completely similar.

Third, the comprehensive information and graphs of Ref. [47] are utilized to validate the results of the present study. The melting of a base PCM was the case study of Ref. [47]. The domain was a square cavity, and the boundary condition included hot/cold left/right vertical walls ($T_h > T_c$), respectively, and horizontal insulated walls. The results depicted in Fig. 6 are captured for $Pr = 50$, $Ra = 12.5 \times 10^4$, and two values of $Fo.\ Ste = 2 \times 10^{-3}$ and 10^{-2}. A good agreement is seen among the results. Finally, in order to validate the natural convective heat transfer behavior within the cavity, the results of Calcagni et al. [48] are examined. They numerically and experimentally studied around the natural convection inside a square cavity that its bottom wall was exposed to a constant heat by a heater and the top wall was adiabatic, and two vertical walls are acting as coolers. According to Fig. 7, a desirable agreement is evident between the temperature distribution inside the cavities for the present study and experimental results of Ref. [48] at $Pr = 0.71$, $\phi = 0.0$, $\varepsilon = 1$ and $Ra = 1.425 \times 10^5$.

4. Results and discussion

The key parameters studied in the current work are the nano-additives volume fraction ($0.0 \le \omega_{na} \le 0.08$), the porosity of porous medium ($0.8\ mm \le \varepsilon \le 1.0\ mm$), the shape of the porous medium (i.e., RHT, LHT, and REC), and the height of the triangular porous medium ($32\ mm \le l_v \le 40\ mm$).

The goal of optimization in this study is to minimize the required time for the experiment. In this respect, "the smaller-the better" category of the Taguchi method is used [49, 50]. The mean values of the signal-to-noise ratios for all the levels of the controlling parameters can be seen in Table 3 and Fig. 8 for the test case of RHT. The optimum levels of controlling parameters are related to the highest values of the S/N ratio of the goal function. Therefore, as reported in Table 6, the corresponding optimal values of the parameters are: $\omega_{na} = 0.08$, $\varepsilon = 0.8$ and $l_v = 32\ mm$. In Table 7, the difference between the maximum value and the minimum value for the three-level values of each controlling parameter is denoted by delta (δ). The higher value of delta δ is associated with a higher influence of the parameter [51, 52]. According to this description, the effectiveness of the parameters can be ranked based on their δ values in the following order: $\varepsilon > \omega_{na} > l_v$. This order demonstrates that parameter ε contributes more to reducing the running time of the experiment when compared to the two other parameters.

Similarly, the results of the Taguchi L9 DOE analysis for the test case of LHT is demonstrated in Fig. 9 and Table (4). As shown in Table 8, the optimal values of the parameters in this case are: $\omega_{na} = 0.08$, $\varepsilon = 0.9$ and $l_v = 40\ mm$. According to Table 9, in this case, the effectiveness of the parameters can be ranked in this order: $\varepsilon > \omega_{na} > l_v$. This order demonstrates that parameter ε contributes more to reducing the running time of the experiment when compared to the two other parameters for

the case of LHT porous medium. The charging time for the optimum case with metal foam was 2575s, while the charging time for a poor design of case 3 is 10400s. Thus, using metal foams, nanoadditives, and optimum geometrical design results in a 3-fold reduction in charging time.

Moreover, the use of the Taguchi method for the last test case (REC) results in the data shown in Table 5 and Fig. 10. The optimum values of $\omega_{na} = 0.08$, $\varepsilon = 0.8$ and $l_v = 8\ mm$ have been obtained in this case (Table 10). Also, in this case, ε has the highest effect and l_v has the lowest effect on reducing the goal function (see Table 11).

The obtained results suggest that, in general, lower melting times are obtained for the case with a triangular porous structure located in contact with the heated wall. In this case, the porous structure covers a larger vertical section of the heated wall as compared to the case where the porous structure is located at the bottom of the container. Therefore, due to the increased contact area and the higher effective thermal conductivity of the porous-PCM, a stronger conduction heat transfer exists at the beginning of the melting process, which accelerates the onset of natural convection. The formation of natural convection has a remarkable effect on the melting rate.

The addition of nanoparticles to the PCM accelerates the melting process by increasing the effective thermal conductivity of the PCM and by decreasing the latent heat of fusion. The effects of nano additives are smaller compared to the other considered parameters, as indicated by the Taguchi method. The dispersion of nanoparticles increases the viscosity, which adversely affects the melting process by suppressing the fluid flow and, hence, natural convection within the molten PCM.

On the other hand, it should be noted that the porosity of the porous insert has a significant influence on the effective thermal conductivity of the composite porous insert-PCM; therefore, it is indicated as the parameter with the highest influence. The porosity of 1 refers to the case with no porous structure. As the porosity decreases, the effective thermal conductivity increases; therefore, a higher rate of heat transfer through the porous regions is expected. However, it should be noted that the porosity also affects the permeability and thereby influences the natural convection mechanism in the melting process. The optimal value of porosity is dependent upon the geometry and configuration of the porous insert.

Regression analysis by Minitab-18 is used to discover the best relationship between the output and the controlling variables in all three test cases [53]. After conducting a nonlinear regression analysis via the Newton Raphson method [54], the regression equation for the test case of RHT is as shown in Eq. (23). Also, Eqs. (24) and (25) show the regression equation for the test case of LHT and REC, respectively.

$$MVF = -19444.44 - -10833.3\omega_{na} + 21000\varepsilon + 218.8l_v \tag{23}$$

$$MVF = -25966.7 - -11041.7\omega_{na} + 34166.7\varepsilon + 18.75lv \tag{24}$$

$$MVF = - - 20856.9 - -5625\omega_{na} + 28291.7\varepsilon + 75.6944lv \tag{25}$$

To better understand the effects of porous structure configuration and location on the melting process, the melting liquid fraction, isotherms, and streamlines are shown in Figs. 11, 12 and 13 for the studied cases. It should be noted that the results are presented for the optimal case of each configuration. Slower melting rates are obtained for the case with the triangular porous matrix located at the right side when compared to the other two cases. As Figs. 12 and 13 illustrate, a 25% melting fraction is obtained after 900 seconds, while the corresponding liquid fraction occurs at $t = 100\ s$ and $t = 150\ s$ for LHT and REC cases. The reason this occurs is because the other two configurations are in contact with the heated wall; therefore, the contact area increases, which causes a faster rate of heat penetration to the PCM. The increased conduction heat transfer triggers an earlier onset of natural convection and a faster growth rate of the recirculation zones. As a larger section of the heated wall is in contact with the porous structure in the LHT case, as compared to the REC configuration, faster melting rates are obtained at the initial stages of the melting process. As shown in Fig. 13, a large circulation zone is formed in the LHT case only 100 seconds after the start of the melting process. The curved isotherms in Fig. 12 also indicate the formation of natural convection in the porous region.

In configuration LHT, the majority of the melting initially occurs inside the porous region. This can be explained by the high thermal conductivity of the porous matrix, hence imposing a lower thermal resistance. The temperature of the PCM is quickly increased above the melting temperature, and melting occurs in a larger portion of the PCM. As shown in Fig. 11, a higher melting rate is also obtained for this stage of the melting process, and the melting liquid fraction plot has a higher slope ($t < 400\ s$). After this stage, the melting rate decreases. The melting in the upper diagonal is now similar to the melting inside a triangular cavity heated along its diagonal and left wall. The isotherm shown in Fig. 12 illustrates how the melting process proceeds for this case. The bending of the isotherms is an indication of the convective flow in the upper region.

In the case of the REC configuration, where a rectangular porous region is located at the bottom, the melting process starts in the porous region due to the same reasons mentioned earlier. In addition, a small layer of the PCM that is in contact with the rest of the heated section is melted. As the melting continues, the melting front is progressing in the porous region and in the upper left corner due to the established natural convection. At $t > 400$ seconds, the melting rates decrease as indicated in Fig. 11, which is likely due to the fact that the majority of the PCM in the porous zone is now melted. After this stage, the melting is similar to a melting process of a rectangular cavity heated from the bottom and left sidewall. The melting process is now assisted by the natural convection recirculation zones formed next to the sidewall and the bottom porous zone.

In configuration RHT, the triangular porous matrix is located in the right diagonal with the objective of accelerating the melting process in that region. It should be noted that the melting process in a cavity heated from the left side, the melting process will progress faster in the left diagonal due to the natural convection. The triangular porous zone is placed in the right diagonal with the aim of accelerating the melting process in this region. Based on the obtained results, this case is not as effective as the other two cases. The study of liquid fraction history reveals that the optimal total melting time decreases by 12.8% and 21.96% as the porous zone configuration changes from the RHT to REC and LHT.

The presence of a metal foam layer greatly enhances thermal conductivity. In the LHT and REC configurations, the metal foam located adjacent to the hot wall drastically increases the heat transfer to the PCM. Hence, the melting rate of the PCM rises until the PCM inside the metal foam fully melts. After that, the PCM inside the clear region (without metal foam) starts to melt. Due to the low thermal conductivity of the PCM, the melting rate decreases. In fact, in these two configurations, the turning point that appeared is due to the different melting rates in the porous and clear zones.

The variation of energy stored and the power (P=ES/t) versus time results are depicted in Fig. 14 for configurations RHT, LHT, and REC. As noted before, the constant surface area of the porous matrix is imposed as the constraint. The results are illustrated for the optimal parameters obtained for each case. For all the cases, the optimal value of the concentration of nanoparticles is 8%. For the RHT and REC configurations, the optimal value of porosity is 0.8, while for the LHT configuration, a porosity of 0.9 will result in the optimal thermal performance. As the density and heat capacity of the selected PCM are greater than the copper foam, a higher porosity will result in a higher heat capacity of the porous-PCM zones; therefore, higher energy stored is the result for the case with an LHT configuration as compared to the other two cases. As the melting time is shorter for configurations LHT and REC, higher energy powers are obtained.

5. Conclusions

The effects of the porous insert configuration on the melting process of a nano-enhanced PCM in a square container was numerically investigated. Three configurations were considered (i.e., right-hand triangle porous medium (RHT), left-hand triangular porous medium (LHT), and rectangular porous medium (REC)), with all the configurations having the same surface area. The Taguchi optimization method was utilized to find the optimal parameters. The optimization was performed with the objective of minimizing the melting time. A lower melting time was obtained for the case with left-hand triangle porous zone when compared to the other two cases. The Taguchi results revealed that the porosity of the porous insert contributes more to decreasing the melting time in comparison to the other two parameters, which were the volume concentration of nano additives and the height of the porous zone. For all the studied configurations, the optimal value of 8% was obtained for the nano additives volume fraction. The optimal porosity of 0.8 was reported for the RHT and REC cases, while this value was found to be 0.9 for configuration LHT. The optimum height for RHT, LHT, and REC cases was found to be 32 *mm*, 40 *mm*, and 8 *mm*, respectively.

Author statement

S.A.M. Mehryan: Conceptualization, Methodology, Software, Validation, Formal analysis, Data Curation. **K. Ayoubi Ayoubloo:** Visualization, Original draft preparation, Investigation. Formal analysis, Data Curation. **M. Mahdavi:** Methodology, Software; Formal analysis, Data Curation. **O. Younis:** Investigation. Formal analysis, Writing - Review & Editing. **Z. Kazemi:** Conceptualization, Formal analysis, Investigation, Writing - Review & Editing. **M. Saidul Islam:** Investigation, Writing - Review & Editing. **O. Younis:** Conceptualization, Writing - Review & Editing, Investigation. **M. Ghodrat:** Writing - Review & Editing, Resources. **M. Ghalambaz**: Investigation, Conceptualization, Methodology, Writing - Review & Editing, Supervision.

Declaration of Competing Interest

The authors clarify that there is no conflict of interest for report.

Acknowledgements

This work was supported by computational resources provided by the Australian Government through University of New South Wales under the National Computational Merit Allocation Scheme.

References

[1] F. Javadi, H. Metselaar, P. Ganesan, Performance improvement of solar thermal systems integrated with phase change materials (PCM), a review, Sol. Energy 206 (2020) 330–352.
[2] N.S. Bondareva, M.A. Sheremet, Conjugate heat transfer in the PCM-based heat storage system with finned copper profile: application in electronics cooling, Int. J. Heat Mass Transfer 124 (2018) 1275–1284.
[3] G. Gholamibozanjani, M. Farid, A comparison between passive and active PCM systems applied to buildings, Renewable Energy 162 (2020) 112–123.
[4] G. Gholamibozanjani, M. Farid, Peak load shifting using a price-based control in PCM-enhanced buildings, Sol. Energy 211 (2020) 661–673.
[5] K. Du, J. Calautit, P. Eames, Y. Wu, A state-of-the-art review of the application of Phase Change Materials (PCM) in Mobilized-Thermal Energy Storage (M-TES) for recovering low-temperature Industrial Waste Heat (IWH) for distributed heat supply, Renewable Energy (2020).
[6] J.M. Mahdi, S. Lohrasbi, E.C. Nsofor, Hybrid heat transfer enhancement for latent-heat thermal energy storage systems: a review, Int. J. Heat Mass Transfer 137 (2019) 630–649.
[7] N.S. Bondareva, N.S. Gibanov, M.A. Sheremet, Computational study of heat transfer inside different PCMs enhanced by Al2O3 nanoparticles in a copper heat sink at high heat loads, Nanomaterials 10 (2) (2020) 284.
[8] N. Jamil, J. Kaur, A. Pandey, S. Shahabuddin, S. Hassani, R. Saidur, R.R. Ali, N.A. C. Sidik, M. Naim, A review on nano enhanced phase change materials: an enhancement in thermal properties and specific heat capacity, J. Adv. Res. Fluid Mech. Therm. Sci. 57 (2019) 110–120.
[9] M. Astanina, M. Sheremet, U. Mahabaleshwar, J. Singh, Effect of porous medium and copper heat sink on cooling of heat-generating element, Energies 13 (10) (2020) 2538.
[10] X. Yang, J. Guo, B. Yang, H. Cheng, P. Wei, Y.-L. He, Design of non-uniformly distributed annular fins for a shell-and-tube thermal energy storage unit, Appl. Energy 279 (2020), 115772.
[11] X. Yang, P. Wei, X. Wang, Y.-L. He, Gradient design of pore parameters on the melting process in a thermal energy storage unit filled with open-cell metal foam, Appl. Energy 268 (2020), 115019.
[12] H.M. Sadeghi, M. Babayan, A. Chamkha, Investigation of using multi-layer PCMs in the tubular heat exchanger with periodic heat transfer boundary condition, Int. J. Heat Mass Transfer 147 (2020), 118970.
[13] H.M. Ali, Applications of combined/hybrid use of heat pipe and phase change materials in energy storage and cooling systems: a recent review, J. Energy Storage 26 (2019), 100986.
[14] M. Sheikholeslami, Numerical modeling of nano enhanced PCM solidification in an enclosure with metallic fin, J. Mol. Liq. 259 (2018) 424–438.
[15] M. Sheikholeslami, Numerical simulation for solidification in a LHTESS by means of nano-enhanced PCM, J. Taiwan Inst. Chem. Eng. 86 (2018) 25–41.
[16] H.I. Mohammed, P. Talebizadehsardari, J.M. Mahdi, A. Arshad, A. Sciacovelli, D. Giddings, Improved melting of latent heat storage via porous medium and uniform Joule heat generation, J. Energy Storage 31 (2020), 101747.
[17] P. Talebizadehsardari, H.I. Mohammed, J.M. Mahdi, M. Gillott, G.S. Walker, D. Grant, D. Giddings, Effect of airflow channel arrangement on the discharge of a composite metal foam-phase change material heat exchanger, Int. J. Energy Res. (2020).
[18] X. Yang, X. Wang, Z. Liu, Z. Guo, L. Jin, C. Yang, Influence of aspect ratios for a tilted cavity on the melting heat transfer of phase change materials embedded in metal foam, Int. Commun. Heat Mass Transfer 122 (2021), 105127.
[19] X. Yang, J. Yu, Z. Guo, L. Jin, Y.-L. He, Role of porous metal foam on the heat transfer enhancement for a thermal energy storage tube, Appl. Energy 239 (2019) 142–156.
[20] D. Zhang, S. Tian, D. Xiao, Experimental study on the phase change behavior of phase change material confined in pores, Sol. Energy 81 (5) (2007) 653–660.
[21] G. Hekimoğlu, M. Nas, M. Ouikhalfan, A. Sarı, V. Tyagi, R. Sharma, Ş. Kurbetci, T. A. Saleh, Silica fume/capric acid-stearic acid PCM included-cementitious composite for thermal controlling of buildings: thermal energy storage and mechanical properties, Energy 219 (2021), 119588.
[22] W. Wu, X. Wang, M. Xia, Y. Dou, Z. Yin, J. Wang, P. Lu, A novel composite PCM for seasonal thermal energy storage of solar water heating system, Renewable Energy 161 (2020) 457–469.
[23] E. Grimonia, M. Andhika, M. Aulady, R. Rubi, N. Hamidah, Thermal management system using phase change material for lithium-ion battery, in: Journal of Physics: Conference Series, IOP Publishing, 2021, 012005.
[24] C. Yadav, R.R. Sahoo, Thermal performance analysis of MWCNT-based capric acid PCM thermal energy storage system, J. Therm. Anal. Calorim. 146 (4) (2021) 1539–1550.
[25] S. Liu, X. Zhang, X. Zhu, S. Xin, A low-temperature phase change material based on capric-stearic acid/expanded graphite for thermal energy storage, ACS Omega 6 (28) (2021) 17988–17998.
[26] H. Fei, W. Du, Q. He, Q. Gu, L. Wang, Study of phase-transition characteristics of new composite phase change materials of capric acid–palmitic acid/expanded graphite, ACS Omega 5 (42) (2020) 27522–27529.
[27] M. Esapour, A. Hamzehnezhad, A.A.R. Darzi, M. Jourabian, Melting and solidification of PCM embedded in porous metal foam in horizontal multi-tube heat storage system, Energy Convers. Manage. 171 (2018) 398–410.
[28] J. Guo, Z. Liu, Z. Du, J. Yu, X. Yang, J. Yan, Effect of fin-metal foam structure on thermal energy storage: an experimental study, Renewable Energy 172 (2021) 57–70.
[29] Z.-Q. Zhu, Y.-K. Huang, N. Hu, Y. Zeng, L.-W. Fan, Transient performance of a PCM-based heat sink with a partially filled metal foam: effects of the filling height ratio, Appl. Therm. Eng. 128 (2018) 966–972.
[30] Y. Xu, M.-J. Li, Z.-J. Zheng, X.-D. Xue, Melting performance enhancement of phase change material by a limited amount of metal foam: configurational optimization and economic assessment, Appl. Energy 212 (2018) 868–880.
[31] D.A. Nield, A. Bejan, Convection in Porous Media, Springer Science & Business Media, 2006.
[32] J. Buongiorno, Convective transport in nanofluids, J. Heat Transfer 128 (3) (2006) 240–250.
[33] M. Sheikholeslami, M. Shamlooei, R. Moradi, Fe3O4-Ethylene glycol nanofluid forced convection inside a porous enclosure in existence of Coulomb force, J. Mol. Liq. 249 (2018) 429–437.
[34] P. Ranut, On the effective thermal conductivity of aluminum metal foams: review and improvement of the available empirical and analytical models, Appl. Therm. Eng. 101 (2016) 496–524.
[35] A. Bhattacharya, V.V. Calmidi, R.L. Mahajan, Thermophysical properties of high porosity metal foams, Int. J. Heat Mass Transfer 45 (5) (2002) 1017–1031.
[36] X. Yang, T.J. Lu, T. Kim, An analytical model for permeability of isotropic porous media, Phys. Lett. A 378 (30–31) (2014) 2308–2311.
[37] X.H. Yang, J.X. Bai, H.B. Yan, J.J. Kuang, T.J. Lu, T. Kim, An analytical unit cell model for the effective thermal conductivity of high porosity open-cell metal foams, Transp. Porous Media 102 (3) (2014) 403–426.
[38] O. Mesalhy, K. Lafdi, A. Elgafy, K. Bowman, Numerical study for enhancing the thermal conductivity of phase change material (PCM) storage using high thermal conductivity porous matrix, Energy Convers. Manage. 46 (6) (2005) 847–867.

[39] H. Zheng, C. Wang, Q. Liu, Z. Tian, X. Fan, Thermal performance of copper foam/paraffin composite phase change material, Energy Convers. Manage. 157 (2018) 372–381.
[40] J.N. Reddy, D.K. Gartling, The Finite Element Method in Heat Transfer and Fluid Dynamics, CRC press, 2010.
[41] O.C. Zienkiewicz, R.L. Taylor, P. Nithiarasu, The finite Element Method for Fluid Dynamics, Elsevier, 2015.
[42] J.C. De Los Reyes, S.González Andrade, A combined BDF-semismooth Newton approach for time-dependent Bingham flow, Numer. Methods Part. Differ. Equ. 28 (3) (2012) 834–860.
[43] O. Schenk, K. Gärtner, Solving unsymmetric sparse systems of linear equations with PARDISO, Future Gen. Comput. Syst. 20 (3) (2004) 475–487.
[44] P. Wriggers, Nonlinear Finite Element Methods, Springer Science & Business Media, 2008.
[45] F. Verbosio, A. De Coninck, D. Kourounis, O. Schenk, Enhancing the scalability of selected inversion factorization algorithms in genomic prediction, J. Comput. Sci. 22 (2017) 99–108.
[46] L. Kumar, B.S. Manjunath, R.J. Patel, S.G. Markandeya, R.G. Agrawal, A. Agrawal, Y. Kashyap, P.S. Sarkar, A. Sinha, K.N. Iyer, S.V. Prabhu, Experimental investigations on melting of lead in a cuboid with constant heat flux boundary condition using thermal neutron radiography, Int. J. Therm. Sci. 61 (2012) 15–27.
[47] O. Bertrand, B. Binet, H. Combeau, S. Couturier, Y. Delannoy, D. Gobin, M. Lacroix, P.Le Quéré, M. Médale, J. Mencinger, H. Sadat, G. Vieira, Melting driven by natural convection A comparison exercise: first results, Int. J. Therm. Sci. 38 (1) (1999) 5–26.
[48] B. Calcagni, F. Marsili, M. Paroncini, Natural convective heat transfer in square enclosures heated from below, Appl. Therm. Eng. 25 (16) (2005) 2522–2531.
[49] M. Ezoddin, J.Å. Jönsson, A. Kyani, Equilibrium sampling through membrane based on a hollow fiber for determination of naproxen and diclofenac in sludge slurry using Taguchi orthogonal array experimental design, Desalin. Water Treat. 52 (13–15) (2014) 2472–2480.
[50] C. Kahraman, S. Yanık, Intelligent Decision Making in Quality Management, Springer, 2016.
[51] S.B. Otieno, C.M. Anderson-Cook, Design and analysis of experiments for directional data, Design and Analysis of Experiments: Special Designs and Applications, John Wiley & Sons, Inc., Hoboken, New Jersey, 2012, pp. 501–532.
[52] K. Hinkelmann, Design and Analysis of Experiments, Volume 3: Special Designs and Applications, John Wiley & Sons, 2012.
[53] T.V. Šibalija, V.D. Majstorović, Advanced Multiresponse Process Optimisation, Springer, 2016.
[54] S.A. Lesik, Applied Statistical Inference with MINITAB®, CRC Press, 2018.
[55] A. Hussanan, M.Z. Salleh, I. Khan, S. Shafie, Convection heat transfer in micropolar nanofluids with oxide nanoparticles in water, kerosene and engine oil, J. Mol. Liq. 229 (2017) 482–488.
[56] K. Kant, A. Shukla, A. Sharma, P.H. Biwole, Heat transfer study of phase change materials with graphene nano particle for thermal energy storage, Sol. Energy 146 (2017) 453–463.